Synthesis of γ-(Al$_{1-x}$Fe$_x$)$_2$O$_3$ solid solutions from oxinate precursors and formation of carbon nanotubes from the solid solutions using methane or ethylene as carbon source

Valdirene G. de Resende[a)]

Department of Subatomic and Radiation Physics, University of Ghent, B-9000 Gent, Belgium; and CIRIMAT UMR CNRS 5085/LCMIE, Centre Interuniversitaire de Recherche et d'Ingénierie des Matériaux, Université Paul-Sabatier, 31062 Toulouse cedex 9, France

Anne Cordier

CIRIMAT UMR CNRS 5085/LCMIE, Centre Interuniversitaire de Recherche et d'Ingénierie des Matériaux, Université Paul-Sabatier, 31062 Toulouse cedex 9, France

Eddy De Grave

Department of Subatomic and Radiation Physics, University of Ghent, B-9000 Gent, Belgium

Alicia Weibel and Alain Peigney

CIRIMAT UMR CNRS 5085/LCMIE, Centre Interuniversitaire de Recherche et d'Ingénierie des Matériaux, Université Paul-Sabatier, 31062 Toulouse cedex 9, France

Geraldo M. da Costa

Chemistry Department, Federal University of Ouro Preto, 35400-000, Ouro Preto (MG), Brazil

Christophe Laurent

CIRIMAT UMR CNRS 5085/LCMIE, Centre Interuniversitaire de Recherche et d'Ingénierie des Matériaux, Université Paul-Sabatier, 31062 Toulouse cedex 9, France

Robert E. Vandenberghe

Department of Subatomic and Radiation Physics, University of Ghent, B-9000 Gent, Belgium

This work reports for the first time the synthesis of γ-(Al$_{1-x}$Fe$_x$)$_2$O$_3$ solid solutions with a high specific surface area (200-230 m^2/g) by the decomposition of metal oxinate [(Al$_{1-x}$Fe$_x$)(C$_9$H$_6$ON)$_3$] and investigated the potential of these materials as catalysts for the synthesis of carbon nanotubes by catalytic chemical vapor deposition using methane or ethylene as carbon the source. The nanocomposite powders prepared by reduction in H$_2$-CH$_4$ contain carbon nanotubes (CNTs), which are mostly double-walled but also contain a fair amount of undesirable carbon nanofibers, hollow carbon particles, and metal particles covered by carbon layers. Moreover, abundant metallic particles are observed to cover the surfaces of the matrix grains. By contrast, the nanocomposite powders prepared by reduction in N$_2$-C$_2$H$_4$ are not fully reduced, and the CNTs are much more abundant and homogeneous. However, they are multiwalled CNTs with a significant proportion of defects. The powders were studied by several techniques including Mössbauer spectroscopy and electron microscopy.

I. INTRODUCTION

Fe-Al$_2$O$_3$ materials are of paramount importance as catalysts for the preparation of carbon nanotubes (CNTs) by catalytic chemical vapor deposition (CCVD) routes. It is generally and rationally conceived that the metal nanoparticles that are active for the catalytic decomposition of

the hydrocarbon are those located at the surface of the matrix grains. One method ensuring that the metal particles do not grow to sizes too large for the catalytic formation of CNTs involves the reduction in H$_2$-CH$_4$ gas atmosphere of alumina-hematite solid solutions, first producing nanometric Fe particles that are active for the decomposition of CH$_4$, thus subsequently producing carbon nanotubes-Fe-Al$_2$O$_3$ nanocomposite powders.[1] A partial substitution of Al^{3+} by Fe^{3+} into the structure of the alumina has therefore been the subject of intensive research, in particular concerning the effects of the characteristics of the precursor material upon the synthesis of

CNTs. Thus, attention was devoted to the influence of the iron content in the precursor material[2] and to the allotropic form and specific surface area of the solid solution.[3,4] To maximize the quantity of CNTs, it is desirable that there are more surface nanoparticles. For a given iron content, this could be achieved by using a starting solid solution with a higher specific surface area (SSA) because this will result in a higher proportion of Fe^{3+} ions located at the surface rather than in the bulk of the oxide grains. Increasing the geometrical surface area by a grinding, which decreases the grain size of the starting powder, was not found[4] to be useful, possibly because the much better packing of the ground powder hampers the supply of CH_4 into the powder bed, which is detrimental to the growth of the CNTs. When using the high-SSA amorphous or transition solid solutions prepared from the mixed-oxalate decomposition and calcination, it was found[3] that some undesirable carbon is entrapped within the Al_2O_3 grains upon the crystallization into the corundum (α) form, which occurs during the reduction step performed at 900 or 1000 °C. Thus, the first part of this work is devoted to the preparation of high-SSA (200–230 m^2/g) γ-$(Al_{1-x}Fe_x)_2O_3$ solid solutions that are more stable and therefore resist the γ-α transformation. We use a novel route based on the decomposition of metal oxinates. Da Costa et al.[5] have reported an alternative soft-chemical method for the synthesis of metal-substituted Fe oxide. They have successfully prepared hematite (α-Fe_2O_3) with Al-for-Fe substitution from metal oxinates obtained by homogeneous precipitation. Other authors have prepared in a similar way Ni- and Zn-doped hematites.[6,7] 8-Hydroxyquinoline (oxine) is a complexing agent that reacts with a variety of cations, producing compounds with general formula $M(C_9H_6ON)_n$ (known as metal oxinate), where M is the cation and n is the valency of the cation, which can be equal to 2, 3, or 4.[8] According to Vogel[8] Al and Fe cations precipitate in approximately the same pH range, i.e., 2.9 and 2.5, respectively. This aspect and the possibility of generating OH^- groups in situ by the decomposition of urea were examined by some authors, e.g., da Costa et al.[5] In a second part of the study, the potential of these solid solutions as catalysts for the synthesis of CNTs by CCVD using methane or ethylene as the carbon source is investigated.

II. EXPERIMENTAL

A. Synthesis of the Al/Fe oxinates and γ-$(Al_{1-x}Fe_x)_2O_3$ oxide powders

Thirty grams of the 8-hydroxyquinoline (C_9H_7NO) were dissolved in 300 ml of acetic acid 3.5 M (20%). Subsequently, ammonium hydroxide was added dropwise until turbidity appeared; the solution was clarified by the addition of a minimal amount of acetic acid. To
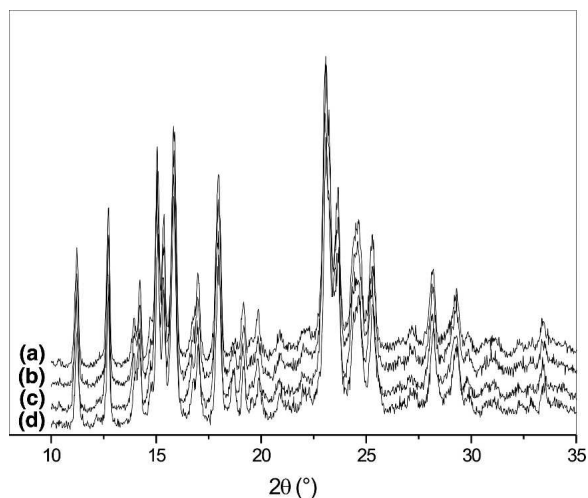
FIG. 1. XRD patterns of the Al/Fe oxinate powders: (a) OxAlFe2, (b) OxAlFe5, (c) OxAlFe7, and (d) OxAlFe10.
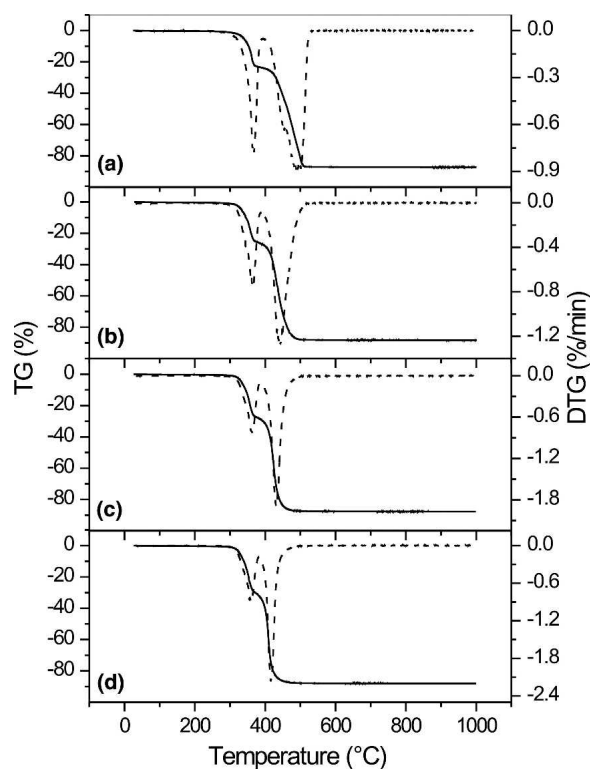
FIG. 2. TGA (solid line) and DTG (dash line) curves for the sample (a) OxAlFe2, (b) OxAlFe5, (c) OxAlFe7, and (d) OxAlFe10.

prepare 2 g of the $(Al_{1-x}Fe_x)_2O_3$ oxide, with x equal to 0.02, 0.05, 0.07 and 0.10, appropriate amounts of $AlNH_4(SO_4)_2.12H_2O$ and $FeNH_4(SO_4)_2.12H_2O$ were dissolved in a mixture of 20 ml of HCl and 1 L of distilled water, using a 2-L flat-bottom boiling flask. Approximately 260 ml of the oxine solution and 70 g of urea were added into the flask, which was connected to a

condenser. This solution was boiled for 2 h. The products were filtered, washed several times with distilled water, and finally dried at 100 °C for 24 h. All Al/Fe oxinates $[(Al_{1-x}Fe_x)(C_9H_6ON)_3]$ are dark green.

Subsequent calcination in air of these products to obtain the oxide solid solutions were performed at 800 °C, a temperature determined by the results of thermal analyses (see below). The oxinate precursors are henceforward named as OxAlFeX, and the fired samples are named as AFX $[\gamma\text{-}(Al_{1-x}Fe_x)_2O_3]$, where X is the cationic % (cat.%) of Fe-for-Al substitution. Four different compositions of $\gamma\text{-}(Al_{1-x}Fe_x)_2O_3$ containing 2, 5, 7, and 10 cat.% of Fe were prepared.

B. Synthesis of carbon nanotubes

CNT-containing nanocomposite powders were prepared by CCVD method. The influence of the carbon source (CH_4 or C_2H_4) was investigated. Several batches of the solid-solution powders containing 2 and 5 cat.% of iron (AF2 and AF5) were reduced in a H_2-CH_4 gas mixture (20 mol% CH_4). The heating and cooling rate to the desired final temperature (1000 °C) and back to room temperature, respectively, was 5 °C/min. No dwell time was applied at 1000 °C. The flowing gas was dried on P_2O_5, and its composition was controlled by mass-flow controllers. The total flow rate was 15 L/h. The so-obtained CNTs-Fe-Al_2O_3 nanocomposite powders are code named AFXRM, where "X" represents the iron content (cat.%) in the starting solid solution and "M" stands for methane. Batches of the γ-alumina-based solid solution containing 2, 5, 7, and 10 cat.% Fe (AF2, AF5, AF7, and AF10) were reduced in a gas mixture of N_2-C_2H_4 (5 mol% C_2H_4). The furnace was heated in two steps. The heating rate was equal to 10 °C/min from room temperature up to 750 °C and 2 °C/min from 750 to 800 °C. At the maximal temperature (800 °C), 1 h of dwell time was applied. The cooling rate to room temperature was equal to 10 °C/min. The flowing gas was dried on P_2O_5 and, its composition was controlled by mass-flow controllers. The total flow rate was 30 L/h. The obtained CNTs-Fe-Al_2O_3 nanocomposite powders are code named

AFXRE, where "X" represents the iron content in the starting solid solution and "E" stands for ethylene.

C. Characterization

Thermogravimetric analysis (TGA) of the oxinates decomposition was performed using approximately 30 mg of each sample in a SETARAM TAG 24 module (simultaneous symmetrical thermoanalyzer). The temperature ranged from 25 to 1000 °C, using a constant flow of synthetic air (25 ml/min) and applying a heating rate of 1 °C/min.

For identification of crystalline phases, x-ray diffraction (XRD) patterns were recorded in the range 10–70° (2θ) using a Bruker D4 Endeavor diffractometer equipped with a Cu K_α radiation tube. Counts were registered every 0.02° (2θ). The background has been subtracted using the EVA software.

The SSA of the oxides was measured by the BET method (Micrometrics Flow Sorb II 2300) using nitrogen

TABLE I. Thermal behavior of the Al/Fe oxinates.

Sample	T_1 (°C)[a]	Weight loss 1 (%)	T_2 (°C)[a]	Weight loss 2 (%)	Total weight loss (%)	Theoretical total weight loss (%)
OxAlFe2	360	23.2	480	63.6	86.8	88.8
OxAlFe5	356	25.6	433	62.2	87.8	88.6
OxAlFe7	354	27.8	422	59.3	87.1	88.5
OxAlFe10	352	30.2	408	57.4	87.6	88.3

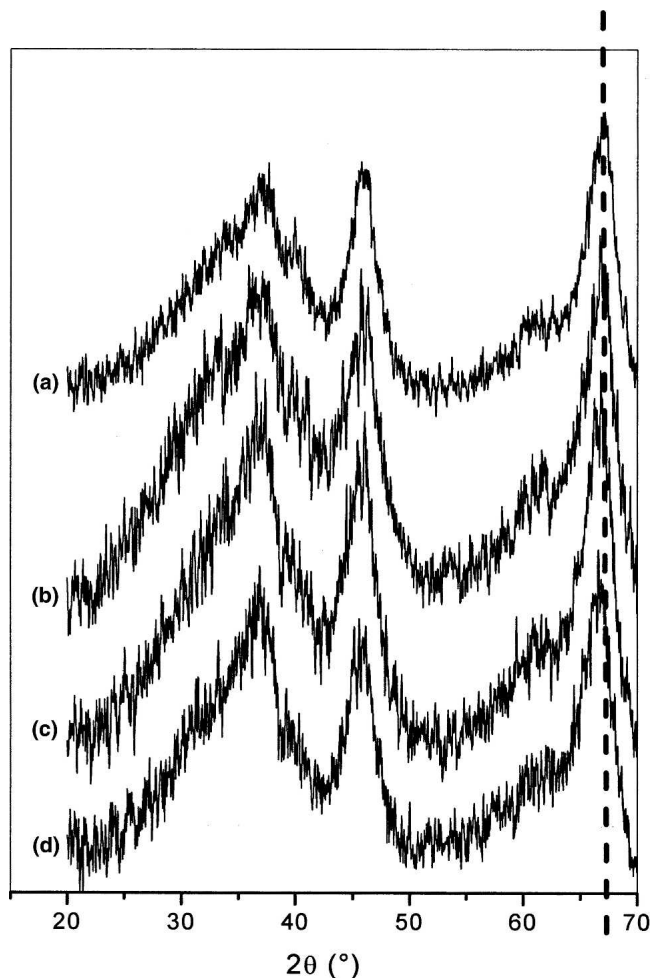[a]Temperature corresponding to minimum in the derivative of the TGA curves (DTG).

FIG. 3. XRD patterns of the γ-alumina-based solid solution: (a) AF2, (b) AF5, (c) AF7, and (d) AF10. The dash line indicates a gradual shift of the peak position at about 67° (2θ).

adsorption at liquid-nitrogen temperature. This instrument gives a SSA value from one point (i.e., one adsorbate pressure) and requires calibration. The reproducibility of the results was determined to be in the ±3% range.

Mössbauer spectra (MS) at 295 and 15 K were collected with a spectrometer operating at constant acceleration mode with triangular reference signal. ^{57}Co(Rh) source was used. The spectrometer has been calibrated by collecting at 295 K the spectrum of a standard metallic iron foil. Isomer shifts are referenced with respect to α-Fe at room temperature.

The carbon content in the nanocomposite samples [C_n (wt%)] was measured by the flash combustion method with an accuracy of ±2%.

Raman spectra were recorded using a LabRAM 800 Jobin-Yvon spectrometer (632.82 nm) and were averaged on three spectra.

Samples of the oxide and the nanocomposite powders were coated with platinum for observation by field-emission-gun SEM equipped with an in-lens electron detector (FEG-SEM, JEOL JSM 6700F). The observations were performed under a tension of 5 kV, and the work distance was in the range 4-6 mm. Transmission electron microscopy (TEM) images were obtained using a JEOL 1011 (100 kV) microscope. The preparation of samples for the TEM imaging involved the dispersion of the powders in ethanol and subsequent deposition on a carbon grid. To study the distribution of the number of walls and the diameter of the CNTs, high-resolution TEM (HRTEM) has been performed using a JEOL JEM 2100F microscope operated at 200 kV. The magnification of the apparatus allowed to clearly resolve the walls of isolated CNTs, which were easily distinguished from other forms of carbon. The powders were slightly sonicated in ethanol to obtain a suitable dispersion without presumably provoking too much damage to the CNTs. A few drops of the suspension were subsequently deposited on a perforated carbon film attached to a copper grid. Only those CNTs that were contained within the holes of the carbon film were probed to avoid any interaction with the support.
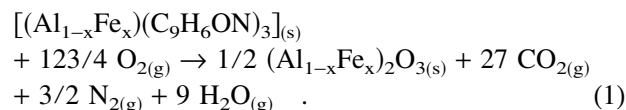
III. RESULTS AND DISCUSSION

A. Al/Fe oxinates

Analysis of the XRD patterns (Fig. 1) of the Al/Fe oxinates show that all the main peaks coincide with those of ε-Al-oxinate as reported by other researchers.[9,10]

Both the pure iron oxinate [$Fe(C_9H_6ON)_3$] and aluminium [$Al(C_9H_6ON)_3$] oxinate have been prepared in earlier years with the aim to perform studies of their thermal stability in air.[11,12] These authors reported that both [$Fe(C_9H_6ON)_3$] and [$Al(C_9H_6ON)_3$] are anhydrous, and that they are fairly stable below 335 and 375 °C, respectively, without weight loss of the sample in those ranges of temperatures. At higher temperatures in air, both iron and aluminium oxinates decompose to produce the respective oxides, i.e., Fe_2O_3 and Al_2O_3. The decomposition of the mixed Al/Fe oxinates can thus be described according to the global reaction [Eq. (1)]:

$$[(Al_{1-x}Fe_x)(C_9H_6ON)_3]_{(s)}$$
$$+ 123/4\ O_{2(g)} \rightarrow 1/2\ (Al_{1-x}Fe_x)_2O_{3(s)} + 27\ CO_{2(g)}$$
$$+ 3/2\ N_{2(g)} + 9\ H_2O_{(g)}\ . \tag{1}$$

The TGA curves and the corresponding differential thermogravimetric (DTG) curves are reported in Fig. 2. No weight loss that could account for dehydration is observed between 25 and 280 °C. Two steps are observed at higher temperatures. The first one starts at 290 °C with a peak position practically unaffected by the iron content ($T_1 = 356 \pm 4$ °C) (Table I). The second step, which slightly overlaps the first one, takes place in a temperature range that is shifted to lower temperatures with increasing iron content (Table I). The peak position T_2 accordingly decreases from 480 °C (OxAlFe2) to 408 °C (OxAlFe10). This observation suggests that the iron ions were indeed coprecipitated with the aluminum ions. Beyond the second stage, the weight remains constant, giving confirmation that the decomposition is completed. For OxAlFe2, the experimental weight loss of the first step (Table I) was calculated to correspond to the loss of 9 mol of carbon for 1 mol of oxinate, producing 9 mol of CO_2, as proposed in reaction [Eq. (2)]. The second step was calculated (Table I) to correspond to the remainder of the decomposition reaction, according to reaction [Eq. (3)].
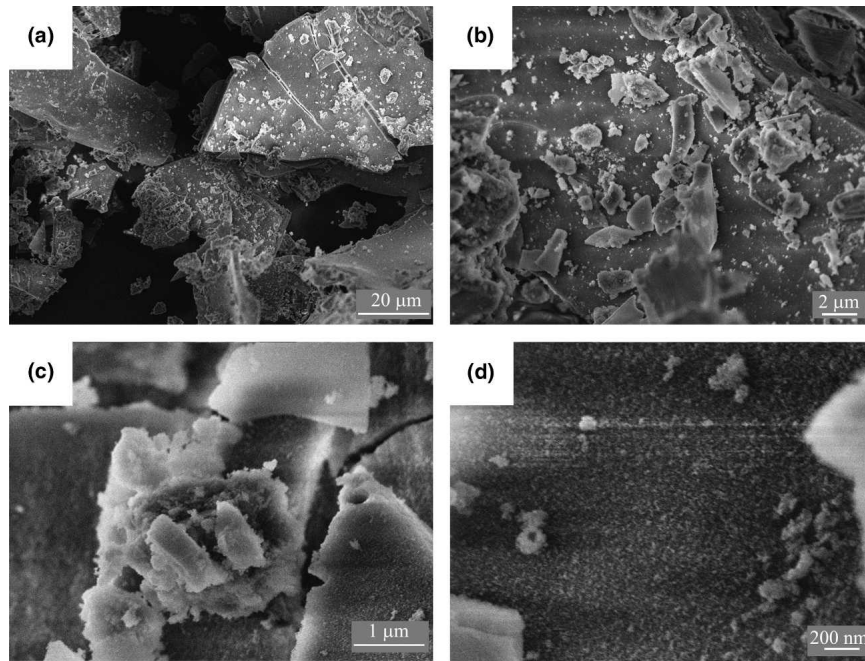

$$\frac{1}{2}\ (Al_{1-x}Fe_x)_2O_3 + 18CO_2 + 9\ H_2O + \frac{3}{2}\ N_2\ . \tag{3}$$
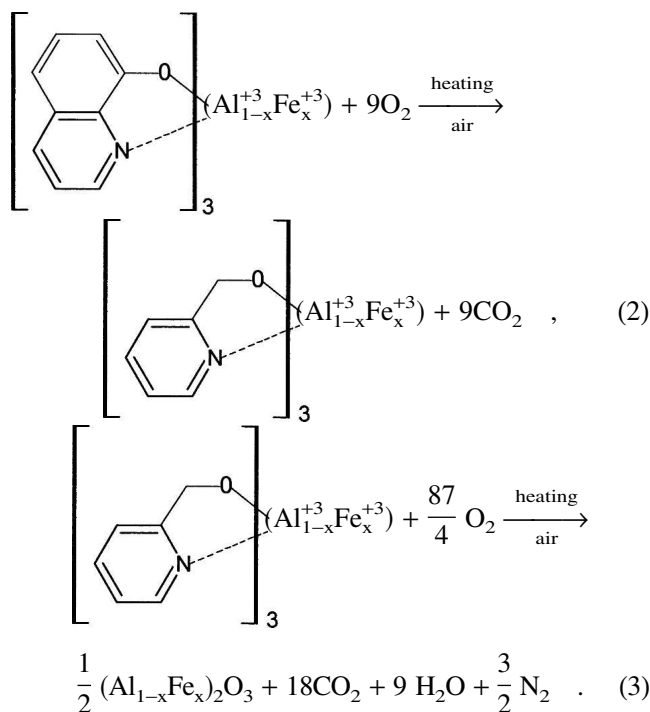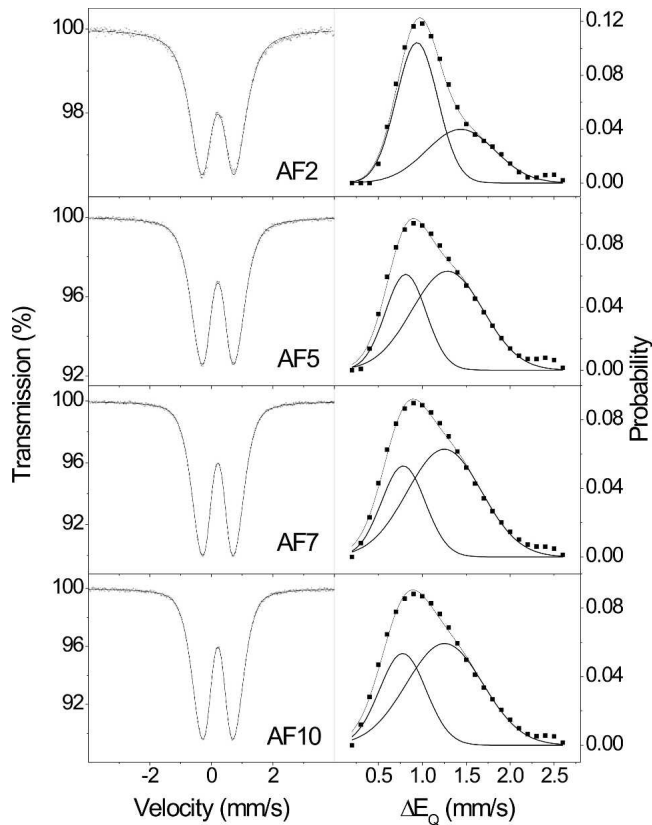
FIG. 4. FEG-SEM images for sample AF5.

FIG. 5. Mössbauer spectra at 295 K of the γ-alumina-based solid solution (left). The probability of distribution is shown on the right side.

TABLE II. Hyperfine parameters at room temperature of γ-alumina solid solution with 2, 5, 7, and 10 cat.% Fe. The values of isomer shifts are with reference to metallic iron at room temperature.

Sample	$\Delta E_{Q,m}$ (mm/s)	δ (mm/s)	$\Delta E_{Q,m,1}$ (mm/s)	RA_1 (%)	$\Delta E_{Q,m,2}$ (mm/s)	RA_2 (%)
AF2	0.98	0.32	0.95	64	1.45	36
AF5	0.92	0.32	0.81	35	1.29	65
AF7	0.92	0.32	0.78	33	1.25	67
AF10	0.91	0.32	0.78	35	1.25	65

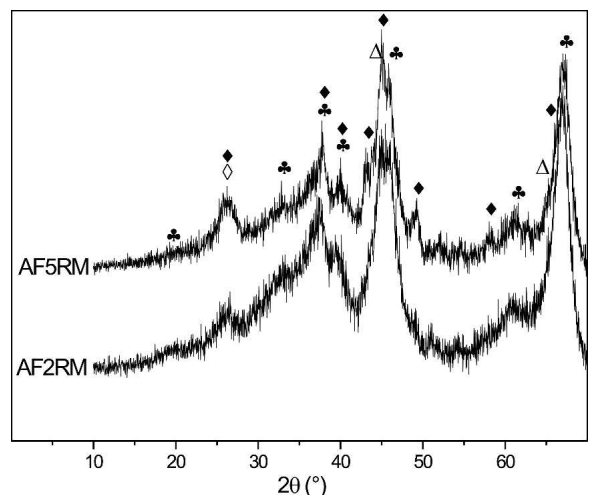$\Delta E_{Q,m,i}$: maximum-probability quadrupole splittings; δ: isomer shifts; RA_i: the relative areas.

FIG. 6. XRD patterns of the nanocomposite powders prepared by reduction in H_2-CH_4. (♣) γ-$(Al_{1-x}Fe_x)_2O_3$; (♦) Fe_3C; (◊) graphite; and (Δ) α-Fe.

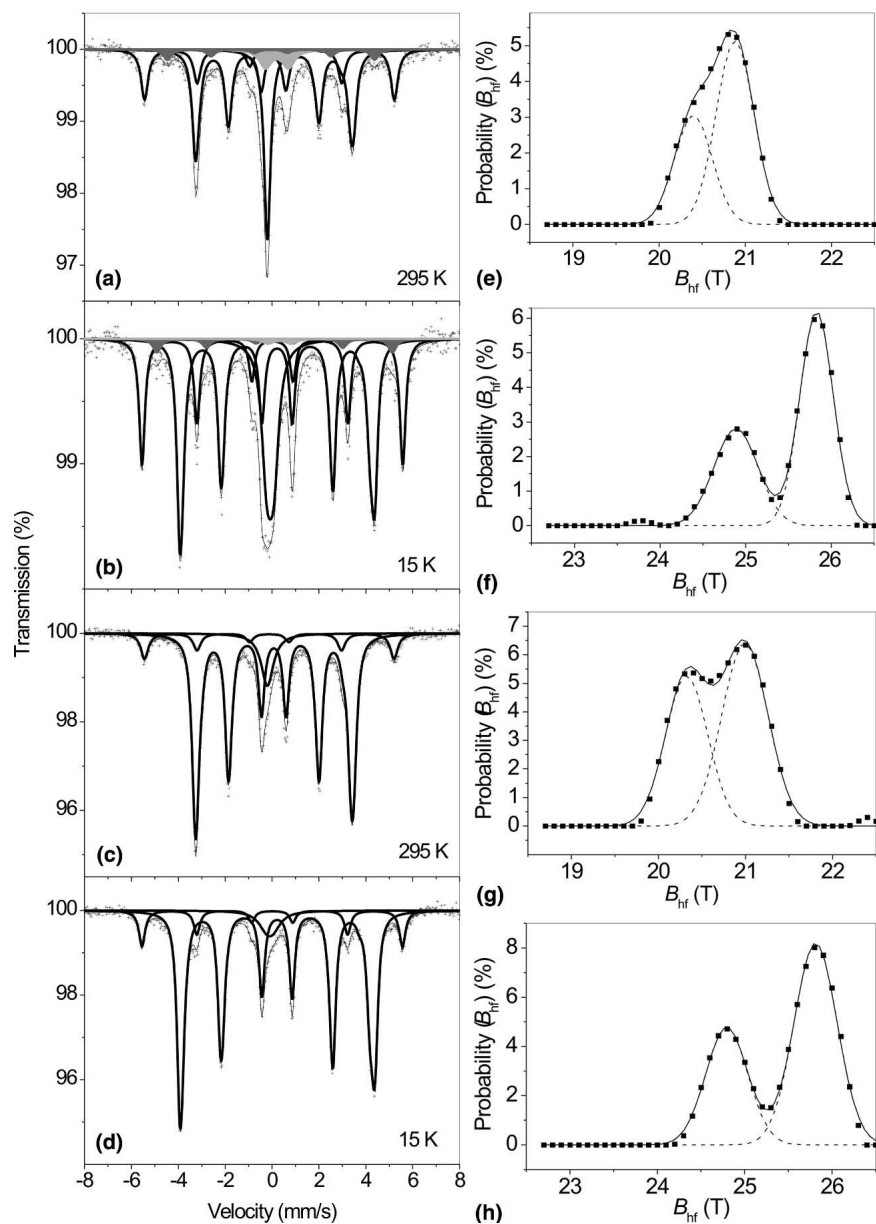The experimental data (Table I) reveal that the proportion of the first step increases at the expense of that of the second one upon increasing the iron content. This

FIG. 7. Mössbauer spectra of the CNTs-Fe-Al$_2$O$_3$ nanocomposite powders prepared by reduction in H$_2$-CH$_4$ measured at 295 and 15 K: (a and b) AF2RM, (c and d) AF5RM, and (e)–(h) corresponding Fe$_3$C hyperfine-field distribution profiles.

trend is in qualitative agreement with what is observed for the pure iron oxinate.[5] However, this evolution should not be observed for the proposed reactions [Eqs. (2) and (3)]. Indeed, both weight losses should slightly diminish upon increasing the iron content. Some basic calculations reveal that the observed difference between the experimental and theoretical data is fairly well correlated with the iron content. This could mean that a part (possibly concerning the breaking of the C–O bond) of what is ascribed as occurring for the second step tends to be more and more occurring for the first one. This observation again supports the coprecipitation of the iron and aluminum ions. The total weight loss as determined

experimentally from the TGA curves are, in average, approximately 1.2% lower than the theoretical values (Table I). This kind of deviation was observed by other authors dealing with oxinate reaction, and an explanation has not been found so far.[5–7] Kumamaru et al.[13] reported that the Al-oxinate is decomposed as opposed to vaporized in the presence of air, whereas it can be volatilized in absence of O$_2$. By contrast, TGA studies performed at 10 °C/min in a flow of synthetic air and giving 100% weight loss with increasing temperature prompted da Costa et al.[5] to suggest that the Al-oxinate is volatile. However, Ribeiro et al.[14] suggested that the relation between the vaporization and the quantity of solid residue

TABLE III. Mössbauer parameters of the nanocomposite powders prepared by reduction in H_2-CH_4 (samples *RM*) measured at 295 and 15 K. The values of isomer shifts are with reference to metallic iron at room temperature.

	α-Fe			Fe$_3$C				γ-Fe-C		
Sample	B_{hf}	δ	RA	B_{hf}^a	$2\epsilon_Q$	δ	RA	B_{hf}	δ	RA
					295 K					
AF2RM[b]	33.0	0.00	22	20.4	0.00	0.17	48		−0.09	19
				20.9	0.02	0.20				
AF5RM	33.0	−0.01	11	20.3	0.00	0.18	80		−0.09	9
				21.0	0.02	0.19				
					15 K					
AF2RM[c]	34.5	0.12	25	24.8	−0.05	0.30	50	1.2	0.03	20
				25.8	0.00	0.32				
AF5RM	34.5	0.12	13	24.8	−0.05	0.31	81	1.2	0.01	6
				25.8	0.01	0.32				

[a]Hyperfine-field distribution from minimal 18.5 T to maximal 26.5 T for all MS.
[b]Also present are a weak sextet with $B_{hf} \approx 27.4$ T, δ ≈ 0.11 mm/s, and RA = 5%, and a weak ferric doublet with $\Delta E_Q = 0.98^*$ mm/s, δ = 0.32* mm/s, and RA = 6%.
[c]Also present is a weak sextet with $B_{hf} \approx 31.1$ T, δ ≈ 0.22* mm/s, and RA = 4%, a weak ferric doublet with $\Delta E_Q = 0.98^*$ mm/s, δ = 0.43* mm/s, and RA = 1%.
*Fixed parameter.
B_{hf}: hyperfine field at the maximum of the distribution (T); $2\epsilon_Q$: quadrupole shift (mm/s); δ: isomer shift (mm/s); *RA*: relative area (%); *T*: temperature (K).
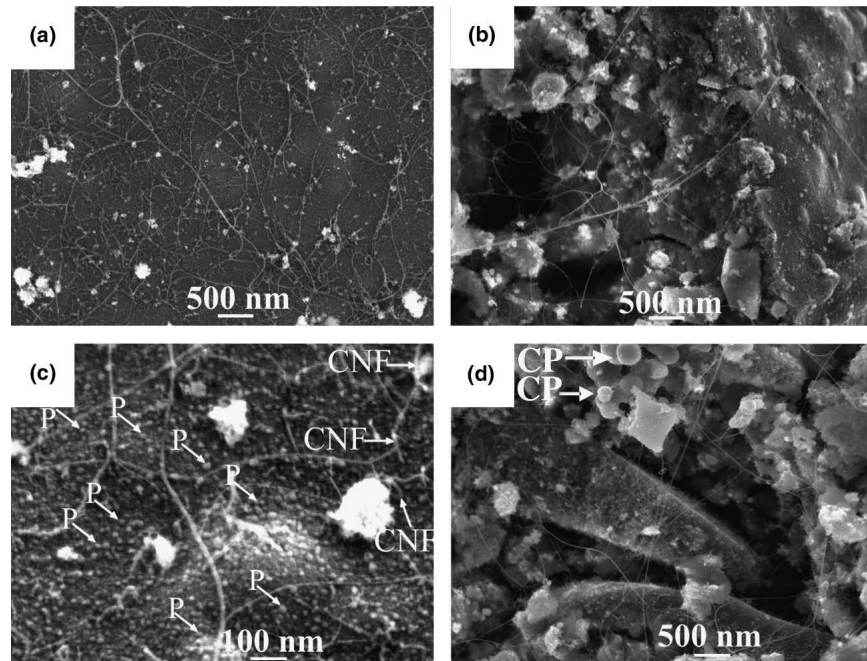

FIG. 8. FEG-SEM images of the CNTs-Fe-Al$_2$O$_3$ nanocomposite powders prepared by reduction in H_2-CH_4: (a and b) AF2RM and (c and d) AF5RM.

depends on the heating rate. As mentioned earlier in this section, the total weight loss was close to 87% for all of the present samples, including the pure aluminum oxinate (not discussed here), thus being in agreement with Ku mamaru et al.[13] As an attempt to shed some light onto this question, additional TGA runs with different heating rates, and masses of samples were performed for the pure Al-oxinate and also for the sample with 2 cat.% Fe. A weight loss of 99% was observed for the run at 50 °C/min and using approximately 3 mg of sample, whereas 92% of loss was observed with a heating rate of 10 °C/min. This confirms the observation by Ribeiro et al.[14] A complete study of these complex phenomena is beyond the scope of this article. A higher heating rate corresponds to a higher rate of input of thermal energy into the reactive specimen, favoring the occurrence of reactions and transformations in a shorter time span. Therefore, if there is a competition between a volatilization and a decomposition,

the instantaneous release of gas molecules by the latter reaction will change the partial pressures if the air flow is not high enough to instantaneously purge the atmosphere. The local conditions may turn in favor of the vaporization until the proper atmosphere is restored. Hence, the inconsistencies described in the literature for the decomposition (temperature, observed weight loss, etc.) might be due to differences in the experimental conditions: heating rate, purge gas flow, mass of sample, and geometry of the sample pan.

B. γ-$(Al_{1-x}Fe_x)_2O_3$ oxide powders

Based on the TGA results, which showed that the decomposition is completed at a temperature below 600 °C, it has been decided to prepare the γ-$(Al_{1-x}Fe_x)_2O_3$ solid solutions by calcination of the powders at 800 °C for 1 h in a preheated furnace. The XRD patterns of the fired materials are shown in Fig. 3. The diffraction peaks are extremely broad, implying a nanosized average crystallite size (~3 nm). The centroids of the peaks are close to the peak positions of the XRD lines of standard γ-Al_2O_3 (PDF card 29-1486). The eventual presence of hematite could not be detected. It seems that there is a gradual shift of all γ-alumina XRD peaks towards lower diffraction angles with increasing iron content, as shown by an inset dash line in Fig. 3. This behavior is expected when ions (Al^{3+}) are replaced by larger ones (Fe^{3+}) in the lattice.

The SSA of the so-obtained γ-$(Al_{1-x}Fe_x)_2O_3$ oxides are in the range 200–230 m^2/g with no apparent influence of the iron content. These values are a confirmation of the small particle size, possibly also reflecting the occurrence of pores. One can note that these values are significantly higher than those (approximately 30 m^2/g) obtained for the η-$(Al_{1-x}Fe_x)_2O_3$ solid solutions prepared by calcination in air at 850 °C of the decomposition products of the corresponding mixed oxalates,[3,15] and they are higher than the values (<128 m^2/g) obtained after calcination at 550 °C of alumina precursors prepared by the combustion route.[16]

FEG-SEM images of a typical powder (AF5) show plate-like particles with a broad size distribution, the maximum being approximately 50 μm [Fig. 4(a)]. The surface of these plates is covered by grains approximately 2 μm in size [Figs. 4(b) and 4(c)], down to less than 50 nm in size [Fig. 4(d)]. The image at higher magnification [Fig. 4(d)] also reveals the nanometric crystallites at the surface of a plate-like particle.

MS were recorded at 295 K for all powders calcined at 800 °C. All spectra consist of a single Fe^{3+} doublet (Fig. 5). All measurements have been done using a narrow velocity scale (±4 mm/s), implying a higher resolution. Note that no hematite was detected, in good agreement with the XRD results. The spectra were fitted with one quadrupole-splitting distribution (QSDs) using a linear correlation between the isomer shift and quadrupole

splitting. The relevant Mössbauer parameters are listed in Table II. The evaluated QSD profiles are plotted on the right side of Fig. 5. The QSD profiles are consistently composed of two distinct maxima for the four involved samples. To quantify the profiles, superpositions of two Gaussian curves were fitted to the evaluated QSD profiles. Each of these Gaussians is characterized by the position of its maximum, $\Delta E_{Q,m,i}$ (i = 1, 2), as reported in Table II. γ-Al_2O_3 is generally considered to be based on a defective spinel structure. The well known, cubic spinel structure (usually denoted as AB_2O_4), has an fcc sublattice of oxygen ions, with A and B cations partially occupying the tetrahedral (T_d) and octahedral (O_h) sites, respectively. The total cation:anion ratio for the spinel structures is 3:4, as opposed to 2:3 in the case of γ-Al_2O_3, thus creating a defective spinel structure because of the vacancies imposed by such an arrangement to maintain the stoichiometry.[17–19] The existence of tetrahedral and octahedral sites in the γ-alumina structure may explain the shape of the QSD profiles as
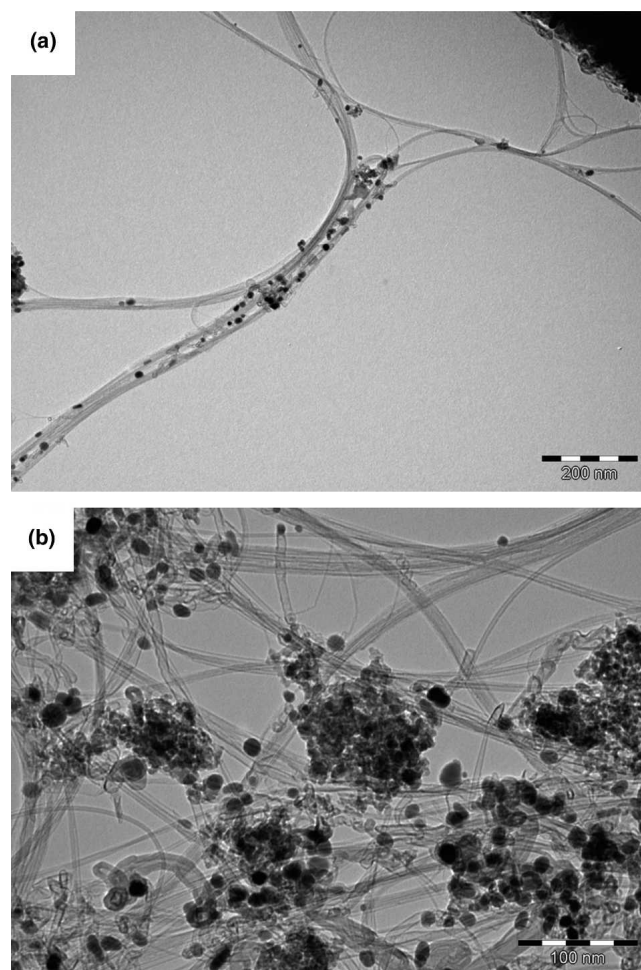

FIG. 9. TEM images for sample AF5RM showing different forms of carbon observed in the nanocomposite powder.
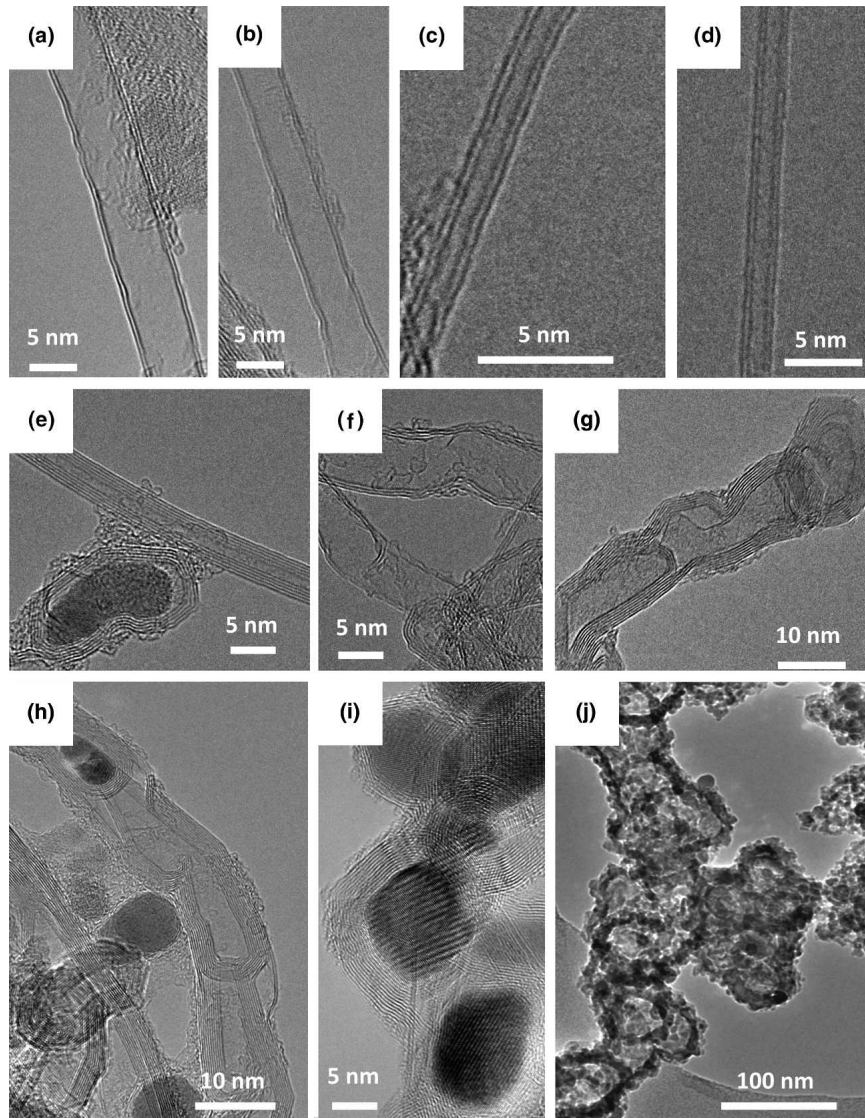
FIG. 10. HRTEM images for sample AF5RM showing different forms of carbon observed in the nanocomposite powder.

evaluated from the MS. But obviously, the presence of two maxima do not give any unambiguous information concerning the site occupancy, i.e., the iron and/or vacancy distribution. Conflicting conclusions are reported in the literature concerning the location and proportion of vacancies in the γ-alumina lattice. It has been mentioned that the vacancies are situated entirely in octahedral positions,[18] entirely in tetrahedral positions,[20] or in both sites. In the latter case, an approximate proportion of 64:36 for the tetrahedral to octahedral coordination was suggested.[21] So far, there is no agreement about the vacancies occupation, although there is a broad consensus that the vacancies do not create a superstructure but appear to be randomly distributed within the unit cell. Because the γ-alumina (spinel structure) has octahedral and tetrahedral lattice sites, it is likely that the Fe^{3+} cations are distributed among these two environments. The

isomer-shift data presented in Table II support this suggestion. For γ-Fe_2O_3 (maghemite, also possessing a defective spinel structure), external-field MS have shown that A-site Fe^{3+} has a δ value of ~0.25 mm/s (295 K), whereas for B-site Fe^{3+} a value of ~0.35 mm/s was found.[22] The presently observed average δ values for the γ-alumina phase are in between these maghemite results. More specific details about the Fe^{3+}-cation distribution in the respective spinel structure cannot be concluded from the present MS.

C. Synthesis of CNTs

1. CNT nanocomposite powders prepared using methane as carbon source

Because the γ-α transition temperature decreases with the increase in the iron content in the solid solution and
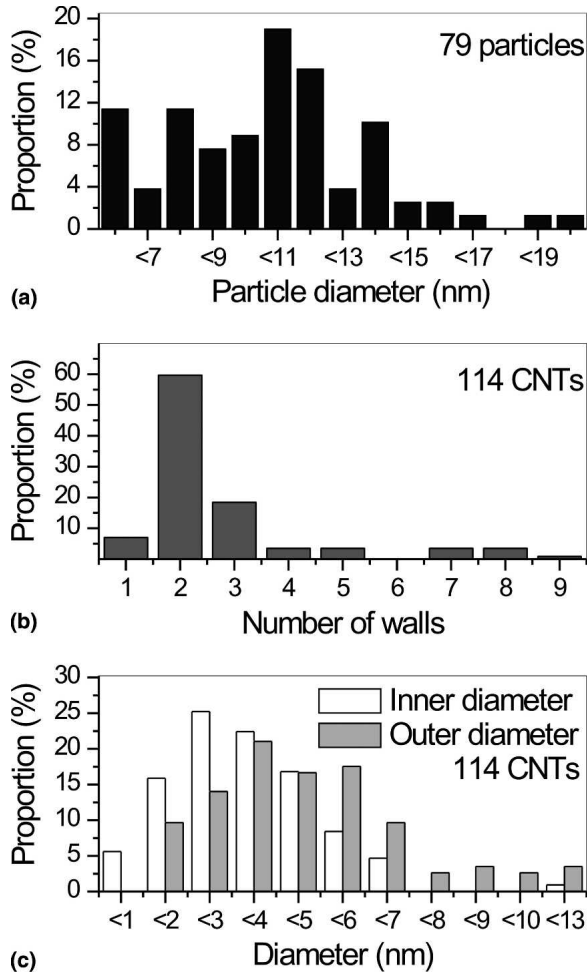
FIG. 11. (a) Particle size, (b) number of walls, and (c) CNT diameter distributions evaluated from HRTEM images of sample AF5RM.

is best avoided to prevent undesirable carbon trapping during the reduction step,[3] only the AF2 and AF5 were reduced in H_2-CH_4 at 1000 °C. Analyses of the XRD patterns (Fig. 6) of the AF2RM and AF5RM nanocomposite powders clearly reveal the presence of α-Fe and Fe_3C (cementite) beside the γ-alumina matrix. It is interesting to note that no α-alumina was detected. It is difficult to clearly separate the patterns of α-Fe and Fe_3C because the respective main diffraction peaks are strongly overlapping. Furthermore, γ-Fe may also be present in the powders, but it cannot be resolved from the XRD patterns because the main γ-Fe (111) diffraction peak ($d_{111} = 0.208$ nm) is probably masked by the γ-alumina peaks, the more so if cementite ($d_{210} = 0.206$ nm) is present as well.[3] The peak at 26° (2θ) that corresponds to the (002) planes of graphite could indicate the possible presence of graphite or of multiwalled CNTs (MWNTs), but it is not feasible to firmly confirm this indication, again because of considerable overlap with diffraction lines of γ-alumina and cementite.

In general, three components were found to be required to obtain adequate fits for the MS at 295 and 15 K (Fig. 7, left) of the nanocomposite powders: (i) an outer sextet due to α-Fe; (ii) an inner asymmetrical six-line pattern that can be ascribed to ferromagnetic cementite; and (iii) a singlet.

For sample AF2RM, an additional, but weak (~5% of total absorption area) and rather ill-defined sextet with hyperfine parameters $\delta \approx 0.11$ mm/s and $B_{hf} \approx 27.4$ T at 295 K, clearly appears in the MS [shaded in gray in Fig. 7(a)] and can be ascribed to an iron carbide phase (Table III). Its hyperfine parameters are indeed in good agreement with those reported by Bauer-Grosse et al.[23] for an amorphous $Fe_{1-y}C_y$ alloy with y = 0.19 ($\delta \approx 0.13$ mm/s and $B_{hf} \approx 27.4$ T at 295 K). In addition, for AF2RM, a weak Fe^{3+} doublet (~6% of the total area) is present in the MS collected at 295 K [shaded in light gray in Fig. 7(a)]. An adequate fit was obtained by fixing this doublet's hyperfine parameters at the values reported in Sec. III. B for γ-alumina solid solution ($\Delta E_Q = 0.98$ mm/s and $\delta = 0.32$ mm/s). Therefore, this doublet can be attributed to a minor amount of Fe^{3+} that has remained within the precursor grains after the reduction treatment.

To resolve the sextet of the α-Fe, single Lorentzian line shapes were used. Its quadrupole shift was forced to be zero. The Mössbauer parameters of α-Fe are those of bulk iron, and no (super)paramagnetic effect is observed. Therefore, particle-size effects are not observed in the obtained Mössbauer parameters. However, particles of small size can be expected. Bødker and Mørup[24] have shown that ultrafine metallic iron particles prepared on a carbon support can exhibit bulk Mössbauer parameters down to a diameter of 2 nm. The present α-iron particles can be compared to the nanoparticles observed in the various CNT-systems such as CNTs-Fe-MgO,[25] CNTs-Fe-MgAl$_2$O$_4$,[26] and CNTs-Fe-Al$_2$O$_3$.[27]

Cementite (Fe_3C) has two inequivalent crystallographic Fe-sites,[28,29] which are magnetically and electronically similar. For the spectra presented in Fig. 7(left), an asymmetry in the cementite six-line patterns is obvious, notably in the MS collected at 15 K: in particular, the first line is deeper and narrower than the sixth line. This observation is in line with the results obtained by Bi et al.,[30] who have shown that the differences between the Mössbauer parameters of the two iron sites of cementite increase with decreasing temperature. Thus, the most reliable fits for the six-line subpatterns of cementite were obtained using hyperfine-field distributions with linear correlations between isomer shift and hyperfine field and between quadrupole shift and hyperfine field. Clearly, two well resolved maxima appear in the calculated distribution profiles (Fig. 7, right), and these beyond any doubt reflect the existence of abovementioned distinct Fe sites. The Mössbauer parameters
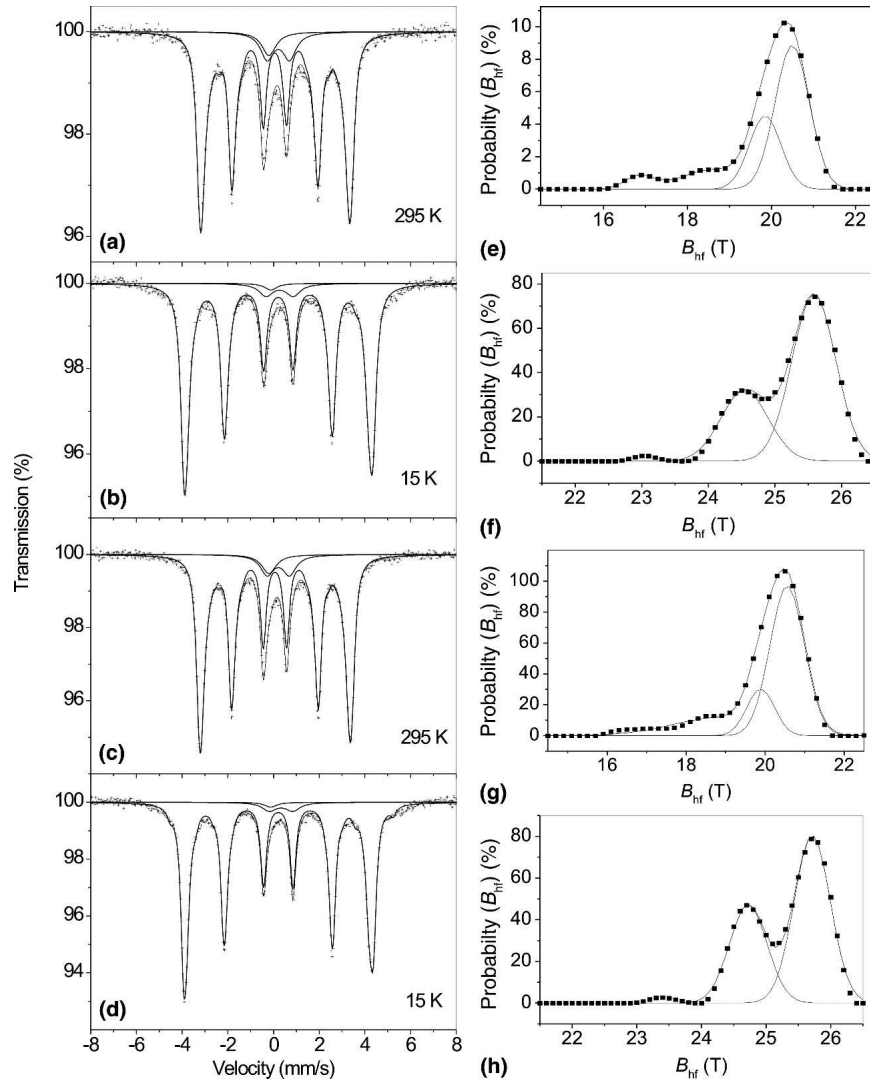
FIG. 12. MS of the CNTs-Fe-Al$_2$O$_3$ nanocomposite powders prepared by reduction in N$_2$-C$_2$H$_4$ measured at 295 and 15 K: (a and b) AF5RE, (c and d) AF10RE, and (e)–(h) corresponding Fe$_3$C hyperfine-field distribution profiles.

corresponding to these two maxima are indeed in excellent agreement with results reported by Bi et al.[30] for nanoparticles of Fe$_3$C measured at room temperature and 12 K.

The total absorption area of the singlet remains, within the experimental error, the same for both at 295 and 15 K, implying no relation with the other phases observed in the MS. A considerable broadening of the singlet is observed at 15 K. For this temperature, a low hyperfine-field sextet was used instead of a singlet to fit the spectra, yielding a more adequate reproduction of the central part of the spectra. This finding implies that the corresponding Fe phase undergoes a magnetic transition at "ultra" low temperature. According to Weiss[31] and Coquay et al.,[26] the isomer shift value of the singlet at 295 K and its broadening at temperatures below 80 K are typical of γ-Fe, which indeed is known to order antiferromagnetically at low temperatures.[32,33] The existence of

a stable antiferromagnetic γ-Fe phase at low temperature can be explained by the presence of carbon atoms in the lattice of the γ-Fe structure and by the small size of the particles as reported by Coquay et al.[26] Indeed, in γ-Fe-C (austenite) the carbon atoms are in the interstitial sites of the fcc γ-structure and, as such, can stabilize the structure at room temperature.[34,35] Kachi et al.[36] reported that the transformation of γ-Fe to α-Fe, which takes place at 910 °C for bulk iron, is hindered in γ-Fe-Ni (with low Ni content) leading to an antiferromagnetic phase at low temperature. This feature seems to be related to the behavior of the small γ-Fe-C particles present in the nanocomposite powders, although in the case of γ-Fe-Ni the Ni atoms are substitutional.

The carbon content (C_n) in the composite AF2RM powder is close to 5.7 wt%, and it is more than double for AF5RM (14.6 wt%). Obviously, the increase of the C_n value is a consequence of the increase of the iron content

TABLE IV. Mössbauer parameters of the nanocomposite powders prepared by reduction in N_2-C_2H_4 (samples *RE*) measured at 295 and 15 K. The values of isomer shifts are with reference to metallic iron at room temperature.

Samples	Fe_3C				Fe^{3+}		
	B_{hf}	$2\epsilon_Q$	δ	RA	ΔE_Q	δ	RA
					295 K		
AF2RE[b]	20.1	0.00	0.17	88	0.98[a]	0.32[a]	8
	20.7	0.02	0.18				
AF5RE[b]	19.9	0.01	0.18	87	0.98[a]	0.32[a]	9
	20.5	0.02	0.18				
AF7RE[b]	20.0	0.01	0.18	89	0.98[a]	0.32[a]	7
	20.7	0.01	0.19				
AF10RE[b]	19.9	0.01	0.18	89	0.98[a]	0.32[a]	7
	20.6	0.02	0.19				
					15 K		
AF2RE[c]	24.7	−0.04	0.30	93	1.01	0.40	6
	25.7	0.01	0.32				
AF5RE[c]	24.5	−0.02	0.30	94	1.19	0.38	5
	25.6	0.00	0.32				
AF7RE[c]	24.7	−0.04	0.30	95	1.17	0.39	4
	25.7	0.01	0.32				
AF10RE[c]	24.7	−0.03	0.31	95	1.03	0.44	4
	25.7	0.00	0.32				

[a]Fixed parameter.

[b,c]A weak singlet due to γ-Fe-C is present. The hyperfine parameters for this phase have been fixed according to values reported by Coquay et al.[26]

B_{hf}: hyperfine field (T); $2\epsilon_Q$: quadrupole shift (mm/s); ΔE_Q: quadrupole splitting (mm/s); δ: isomer shift (mm/s); RA: relative area (%); T: temperature (K).

in the starting solid solution, in line with earlier studies,[2] because more catalytic particles will be available for the decomposition of methane. The high-frequency range (1100–1800 cm^{-1}) of the Raman spectra (data not shown) shows the D band (~1328 cm^{-1}) and the G band (~1580 cm^{-1}) with a shoulder at higher frequency (~1605 cm^{-1}). This shoulder is typical of defective graphite-like materials and is usually observed for MWNTs.[37] The shoulder is more intense for AF5RM than for AF2RM. Accordingly, the ratio between the intensity of the D band and the G band, $I_{D/G}$, is higher for AF5RM than for AF2RM (132 and 57%, respectively). An increasing $I_{D/G}$ value corresponds to a higher proportion of sp^3-like carbon, which is generally attributed to the presence of more structural defects. The presence of radial-breathing-modes (RBM) peaks in the low-frequency range (100–300 cm^{-1}) of the spectrum, the frequencies of which are inversely proportional to the CNT diameters, is usually the sign of the presence of small-diameter CNTs, such as single- and double-walled CNTs (SWNTS and DWNTs, respectively). Only weak RBM peaks are observed for the present specimens. Note however that the Raman process is influenced by optical resonance, and it is thus impossible to detect all of the present CNTs using only one wave length. Moreover, the peak intensities do not reflect the real amount of individual CNT because of the resonance effect, which amplifies the Raman signal from certain CNT.

FEG-SEM images of AF2RM reveal the presence of long, flexible filaments, with a smooth and regular surface, on the surface of the oxide grains [Fig. 8(a)] and bridging several grains [Fig. 8(b)]. All filaments have a diameter smaller than 30 nm and a length of the order of some tens of micrometers. From the results of previous studies, it is known that such filaments are isolated CNTs and/or CNTs bundles. Spherical particles, which may be α-Fe, γ-Fe, and/or Fe_3C, are observed at the matrix surface [some of which are labeled P on Fig. 8(c)]. The diameter of these particles ranges between 5 and 20 nm. Most of these particles do not appear to be connected to a CNT, indicating that they have been inactive for the formation of CNT in the present experimental conditions. Moreover, the presence of thick, short carbon nanofibers [labeled CNF on Fig. 8(c)] is observed. Such CNF are similar to some species commonly observed in works on filamentous carbon.[38] The formation mechanisms are different from those thought to occur in the case of CNTs.[39] FEG-SEM images of AF5RM are similar, but more CNF are observed. Some groups of large carbon particles (up to 300 nm in diameter) [labeled CP on Fig. 8(d)] are observed. How they were formed is unclear.

Typical TEM images collected for sample AF5RM are shown in Fig. 9. Bundles of CNTs, CNF, and metallic particles are observed. Typical HRTEM images for the various species are shown in Fig. 10. DWNTs with a diameter either higher or lower than 5 nm are shown in Figs. 10(a) and 10(b) and Figs. 10(c) and 10(d), respectively. A CNT with five walls and a particle within a shell formed of several graphene layers are shown in Fig. 10(e). Figure 10(f) reveals the defects present in some large diameter CNTs. Bamboo-like CNFs, empty or partly filled with a metal particle, are shown in Figs. 10(g) and 10(h). Particles within shells formed of many graphene layers, approximately 10 nm in diameter, are shown in Fig. 10(i). Large, hollow carbon particles that appear to be poorly organized are shown in Fig. 10(j). Figure 11 presents histograms of the (a) particle size, (b) number of walls, and (c) diameter distribution of the CNTs, which were obtained by measuring nanoparticles and CNTs on similar HRTEM images for sample AF5RM. The particles size falls in the range 5–20 nm, revealing an average diameter of ~10 nm [Fig. 11(a)]. Theoretical and experimental results have shown that CNTs are produced by catalytic particles below 3–6 nm in diameter, whereas particles in the size range approximately 6–10 nm are encapsulated by carbon layers, and the larger ones produce nanofibers, short filaments, and bamboos.[27,40–42] Therefore, the large majority of metallic particles observed in the present samples are those
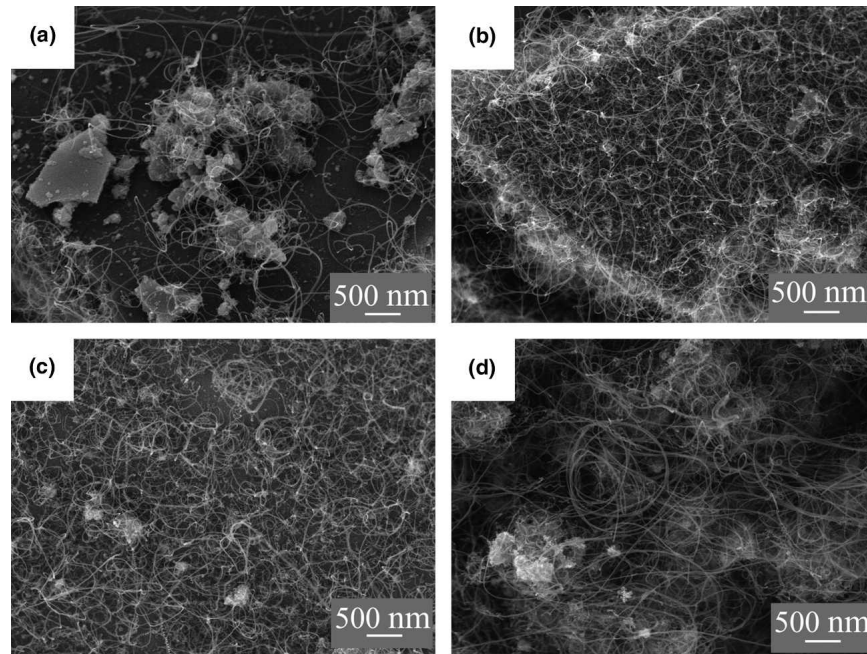
FIG. 13. SEM images of the CNTs-Fe-Al$_2$O$_3$ nanocomposite powders prepared by reduction in N$_2$-C$_2$H$_4$: (a) AF2RE, (b) AF5RE, (c) AF7RE, and (d) AF10RE.
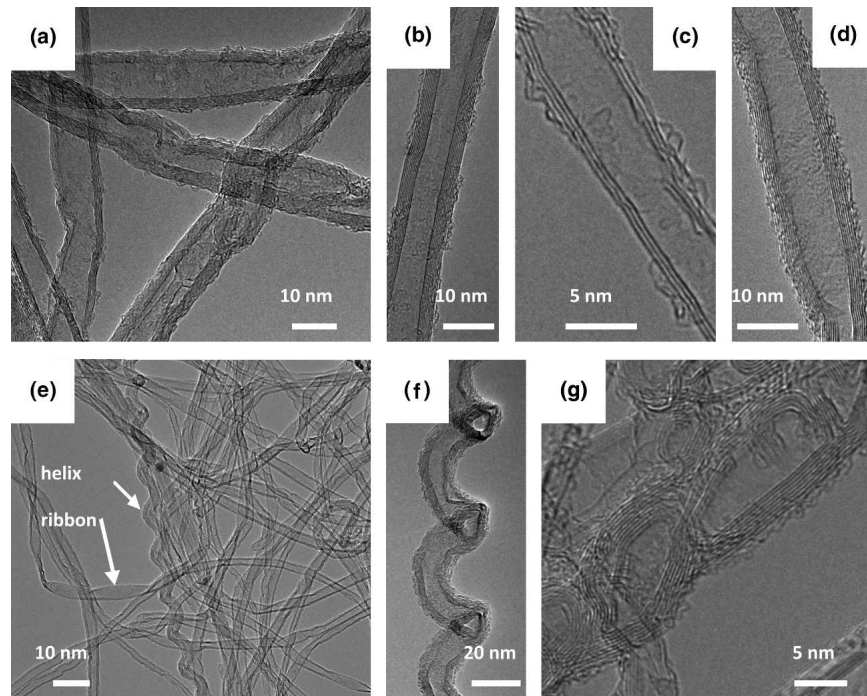

FIG. 14. HRTEM images for sample AF5RE showing different forms of carbon observed in the nanocomposite powder.

actually expected to be too large to produce CNTs. The distribution of the number of walls [Fig. 11(b)] shows that most of CNTs are DWNTs and triple-walled CNTs (3WNTs), their total abundance being 78%. The width of the diameter distributions for all measured CNTs exhibit broad ranges, the averages being ~3.3 and ~4.7 nm for the inner and outer diameter, respectively [Fig. 11(c)].

Combining the SEM and TEM results for both AF2RM and AF5RM samples, it can be inferred that a substantial amount of large metallic particles at the surface of the matrix grains have been formed during the reduction and thus have not been active for CNT formation, but rather for the formation of undesirable carbon species. Whatever the iron content used in the present study, the

reduction of the Fe^{3+} ions of the γ-$(Al_{1-x}Fe_x)_2O_3$ solid solutions, producing iron nanoparticles, occurs at a temperature that is too low for the catalytic decomposition of methane to take place at the surface of the so-obtained nanoparticles. Thus, most nanoparticles are able to grow, the more so for a higher iron content, because there is no (or too little) solid carbon deposited at their surface to block the process. When the catalytic decomposition of methane does take place at the surface of the nanoparticles, the smaller ones indeed produce a CNT, but the larger ones do not, rather they produce a CNF or become fully covered by graphene layers. Thus, the use of a carbon source, ethylene, that is able to decompose at a lower temperature than methane will be investigated in the next section.

2. CNT nanocomposite powders prepared using ethylene as carbon source

In the following part of the study, we attempted to perform the reduction at a lower temperature (800 °C), using N_2-C_2H_4 atmosphere. As mentioned above, ethylene decomposes at a lower temperature than methane, and, moreover, a lower reduction rate of the Fe^{3+} ions would produce, for a given time, a lower amount of metallic phase, which would also favor the formation of smaller Fe particles. The XRD patterns (data not shown) of the AF2RE, AF5RE, AF7RE, and AF10RE nanocomposite powders showed essentially the diffraction peaks due to γ-alumina. The presence of Fe and Fe_3C is not confirmed unequivocally due to the overlapping with the diffraction lines of the γ-alumina. Graphite and/or MWNTS may be present as well.

Three components were found to be necessary to fit the MS: (i) an asymmetrical sextet ascribed to Fe_3C; (ii) a Fe^{3+} doublet; and (iii) a singlet due to γ-Fe-C. It is interesting to note that no α-Fe was found, probably because the reduction atmosphere contains no H_2. Examples of the MS at 295 and 15 K are shown in Fig. 12, for samples AF5RE and AF10RE, respectively. The hyperfine parameters for all of the samples are listed in Table IV. The Fe^{3+} doublet was assumed to be due to the Fe^{3+} ions present in the structure of the unreacted γ-alumina. Some restrictions had to be imposed for the interaction procedure to reach convergency with reasonable parameter values. These restrictions are specified in the footnotes to Table IV. The single line present in the spectra was attributed to γ-Fe-C. The RA of the singlet is merely less than 5% at room temperature. To obtain a better fit of the spectra, the hyperfine parameters for γ-Fe-C component had to be fixed in values reported in Sec. III. C. 1. Due to the small contribution of the γ-Fe-C and Fe^{3+} components, the Mössbauer parameters are extremely ill-defined, and no further attention has been paid to them.

The carbon content increases upon the increase of the

iron content in the solid solution (33.5, 39.8, 48.5, and 53.0 wt% for AF2RE, AF5RE, AF7RE, and AF10RE, respectively). It is interesting to note that these values are much higher than those obtained when using methane (5.7 and 14.6 wt% for AF2RM and AF5RM, respectively). A similar result has been obtained when using other catalysts.[43,44]

FEG-SEM images (Fig. 13) revealed that the powders prepared by reduction in N_2-C_2H_4 are different and much more homogeneous than those prepared by reduction in H_2-CH_4. Indeed, the matrix grains are covered by a web-like network of carbon filaments not larger than 60 nm in diameter and several tens of micrometers long. The quantity of filaments increases with the increase in the content of iron. HRTEM images (Fig. 14) revealed that the filaments, most of which have a diameter lower than 15 nm, are MWNTs with many defects in the walls structure [Figs. 14(a) and 14(b)]. Disordered carbon is observed at the surface, but most of it is formed during the observation because the CNTs, notably the thinner [Fig. 14(c)], are damaged by the electron beam. Some ribbons [Figs. 14(d) and 14(e)], helix-shaped CNTs [Figs. 14(e) and 14(f)], and carbon particles, sometimes arranged as bamboo-nanofibers [Fig. 14(g)], are observed too. These observations are in good agreement with the results reported by other authors using ethylene as the carbon source and different catalytic materials.[43,45–48]

Raman spectra (data not shown) show the D and G bands but no RBM. The $I_{D/G}$ values calculated from the spectra are high (approximately 135%) for all powders. This is slightly higher than the values reported by Qian et al.,[49] but it is in good agreement with the present electron microscopy observations. Interestingly, McCaldin et al.[50] showed, using a different catalytic material, that the formation of the various carbon forms (platelet nanofibers, herringbone nanofibers, MWNTs, and encapsulated metal particles) strongly depends on the temperature and gas mixture composition. The present reduction conditions applied on the γ-$(Al_{1-x}Fe_x)_2O_3$ solid solutions already produce mostly MWNTs. Fine-tuning them could yield higher-quality MWNTs.

IV. CONCLUSIONS

This work reported for the first time the synthesis of γ-$(Al_{1-x}Fe_x)_2O_3$ solid solutions with a high specific surface area (200-230 m^2/g) by the decomposition of metal oxinate $[(Al_{1-x}Fe_x)(C_9H_6ON)_3]$ at 800 °C and the preparation of CNT nanocomposite powders from these solid solutions using methane or ethylene as the carbon source. The Mössbauer spectroscopy results showed that for the present γ-alumina (spinel structure) samples, the Fe^{3+} cations are distributed among the octahedral and tetrahedral lattice sites. More specific results of the Fe^{3+} proportions on the two respective environments could

not be inferred by the presented Mössbauer results because its isomer shift values are similar. The potential of these solid solutions as catalysts for the synthesis of carbon nanotubes by CCVD is then investigated. As evidenced by the Mössbauer spectroscopy results, 1000 °C is a high enough temperature to reduce all Fe^{3+} ions substituting the γ-$(Al_{1-x}Fe_x)_2O_3$-based solid solution to metallic state in the H_2-CH_4 atmosphere with 20 mol% CH_4, with the exception of the sample with the lower iron content (x = 0.02). The proportions of γ-Fe-C remain more or less constant, whereas the proportions for the other components (α-Fe and Fe_3C) vary from one powder to another. The nanocomposite powders prepared by reduction in H_2-CH_4 at 1000 °C contain CNTs which are mostly double-walled but also a fair amount of undesirable carbon nanofibers, hollow carbon particles, and metal particles covered by carbon layers. Moreover, abundant metallic particles are observed to cover the surface of the matrix grains. The reduction of the Fe^{3+} ions of the γ-$(Al_{1-x}Fe_x)_2O_3$ solid solutions occurs at a temperature that is too low for the catalytic decomposition of methane to take place at the surface of the so-obtained iron nanoparticles. So the amount of solid carbon is insufficient to block the growth of the iron nanoparticles and to induce the nucleation of CNTs. By contrast, the nanocomposite powders prepared by reduction in N_2-C_2H_4 at 800 °C are not fully reduced, and the CNTs are much more abundant and homogeneous. However, they are mostly MWNTs with a significant proportion of defects. Work is in progress to fine-tune the N_2-C_2H_4 reduction conditions to increase the selectivity towards higher-quality MWNTs.

ACKNOWLEDGMENTS

REFERENCES

1. A. Peigney, Ch. Laurent, F. Dobigeon, and A. Rousset: Carbon nanotubes grown in situ by a novel catalytic method. *J. Mater. Res.* **12,** 613 (1997).
2. A. Peigney, Ch. Laurent, O. Dumortier, and A. Rousset: Carbon nanotubes-Fe-alumina nanocomposites. Part I: Influence of the Fe content on the synthesis of powders. *J. Eur. Ceram. Soc.* **18,** 1995 (1998).
3. Ch. Laurent, A. Peigney, and A. Rousset: Synthesis of carbon nanotubes-Fe-Al_2O_3 nanocomposite powders by selective reduction of different $Al_{1.8}Fe_{0.2}O_3$ solid solutions. *J. Mater. Chem.* **8,** 1263 (1998).
4. Ch. Laurent, A. Peigney, E. Flahaut, and A. Rousset: Synthesis of carbon nanotubes-Fe-Al_2O_3 powders. Influence of the characteristics of the starting $Al_{1.8}Fe_{0.2}O_3$ oxide solid solution. *Mater. Res. Bull.* **35,** 661 (2000).
5. G.M. da Costa, E. Van San, E. De Grave, R.E. Vandenberghe, V. Barrón, and L. Datas: Al hematites prepared by homogeneous precipitation of oxinates: Material characterization and determination of the Morin transition. *Phys. Chem. Miner.* **29,** 122 (2002).
6. C.A. Barrero, J. Arpe, E. Sileo, L.C. Sánchez, R. Zysler, and C. Saragovi: Ni- and Zn-doped hematite obtained by combustion of mixed metal oxinates. *Physica B (Amsterdam)* **354,** 27 (2004).
7. C. Saragovi, J. Arpe, E. Sileo, R. Zysler, L.C. Sánchez, and C.A. Barrero: Changes in the structural and magnetic properties of Ni-substituted hematite prepared from metal oxinates. *Phys. Chem. Miner.* **31,** 625 (2004).
8. A.I. Vogel: *A Textbook of Quantitative Inorganic Analysis*, 3th ed. (Longman Group Limited, London, 1961), p. 387.
9. M. Rajeswaran and T. Blanton: Single-crystal structure determination of a new polymorph (ϵ-Alq_3) of the electroluminescence OLED (organic light-emitting diode) material, tris(8-hydroxyquinoline) aluminum (Alq_3). *J. Chem. Crystallogr.* **35,** 71 (2005).
10. R. Katakura and Y. Koide: Configuration-specific synthesis of the facial and meridional isomers of tris(8-hydroxyquinolinate) aluminum (Alq_3). *Inorg. Chem.* **45,** 5730 (2006).
11. M. Borrel and R. Pâris: Thermogravimetric analysis of the principal metal oxinates. *Anal. Chim. Acta* **4,** 267 (1950).
12. O.G. Palanna: Thermal studies of ferric oxinate. *Chim. Acta Turc.* **25,** 25 (1997).
13. T. Kumamaru, H. Notake, S. Tao, and Y. Okamoto: Low temperature electrothermal vaporization of an 8-quinolinolato complex of aluminum (III) for sample introduction in an inductively coupled plasma atomic emission spectrometric determination of trace aluminum. *Anal. Sci.* **13,** 885 (1997).
14. C.A. Ribeiro, M.S. Crespi, C.T.R. Guerreiro, and A.M. Veronezi: Dehydratation and volatilization non isothermic kinetic of the solid state aluminum 8-hydroxyquinolinate. Eclet. *Quím.* **26,** 185 (2001).
15. X. Devaux: Nanocomposites as ceramic matrices. Systems aluminum-transition metal (iron, chromium) and aluminum iron-chromium alloys. Doctoral Thesis, Toulouse, 1991, p. 166.
16. A. Cordier, A. Peigney, E. De Grave, E. Flahaut, and Ch. Laurent: Synthesis of the metastable α-$Al_{1.8}Fe_{0.2}O_3$ solid solution from precursors prepared by combustion. *J. Eur. Ceram. Soc.* **26,** 3099 (2006).
17. F.H. Streitz and J.W. Mintmire: Energetics of aluminum vacancies in gamma alumina. *Phys. Rev. B* **60,** 773 (1999).
18. C. Wolverton and K.C. Hass: Phase stability and structure of spinel-based transition aluminas. *Phys. Rev. B* **63,** 024102 (2000).
19. H.P. Pinto, R.M. Nieminem, and S.D. Elliott: Ab initio study of γ-Al_2O_3 surfaces. *Phys. Rev. B* **70,** 125402 (2004).
20. G. Gutiérrez, A. Taga, and B. Johansson: Theoretical structure determination of γ-Al_2O_3. *Phys. Rev. B* **65,** 012101 (2001).
21. L.J. Alvarez and L.E. León: Surface structure of cubic aluminum oxide. *Phys. Rev. B* **50,** 2561 (1994).
22. G.M. da Costa, E. De Grave, and R.E. Vandenberghe: Mössbauer studies of magnetite and Al-substituted maghemites. *Hyperfine Interact.* **117,** 207 (1998).
23. E. Bauer-Grosse, G. Le Caër, and L. Fournes: Mössbauer study of amorphous and crystallized $Fe_{1-x}C_x$ alloys. *Hyperfine Interact.* **27,** 297 (1986).
24. F. Bødker and S. Mørup: Magnetic properties of 2 nm α-Fe particles. *Hyperfine Interact.* **93,** 1421 (1994).

25. P. Coquay, A. Peigney, E. De Grave, R.E. Vandenberghe, and Ch. Laurent: Carbon nanotubes by a CCVD method. Part II: Formation of nanotubes from (Mg,Fe)O catalysts. *J. Phys. Chem. B* **106,** 13199 (2002).

26. P. Coquay, E. De Grave, R.E. Vandenberghe, C. Dauwe, E. Flahaut, Ch. Laurent, A. Peigney, and A. Rousset: Mössbauer spectroscopy study of $MgAl_2O_4$-matrix nanocomposite powders containing carbon nanotubes and iron-based nanoparticles. *Acta Mater.* **48,** 3015 (2000).

27. A. Peigney, P. Coquay, E. Flahaut, R.E. Vandenberghe, E. De Grave, and Ch. Laurent: A study of the formation of single-and double-walled carbon nanotubes by a CVD method. *J. Phys. Chem. B* **105,** 9699 (2001).

28. H.L. Yakel: Crystal structures of stable and metastable iron containing carbides. *Int. Met. Rev.* **30,** 17 (1985).

29. B. Kniep, A. Constantinescu, D. Niemeier, and K.D. Becker: An in-situ Mössbauer study of the formation of cementite, Fe_3C. *Z. Anorg. Allg. Chem.* **629,** 1795 (2003).

30. X.X. Bi, B. Ganguly, G.P. Huffman, F.E. Huggins, M. Endo, and P.C. Eklund: Nanocrystalline α-Fe, Fe_3C, and Fe_7C_3 produced by CO_2 laser pyrolysis. *J. Mater. Res.* **8,** 1666 (1993).

31. R.J. Weiss: The origin of the "invar" effect. *Proc. Phys. Soc.* **82,** 281 (1963).

32. U. Gonser, C.J. Meechan, A.H. Muir, and H. Wiedersich: Determination of Néel temperatures in fcc iron. *J. Appl. Phys.* **34,** 2373 (1963).

33. L.A. Warnes and H.W. King: The low temperature magnetic properties of austenitic Fe-Cr-Ni alloys. 2. The prediction of Néel temperatures and maximum susceptibilities. *Cryogenics* **16,** 659 (1976).

34. C.S. Roberts: Effect of carbon on the volume fractions and lattice parameters of retained austenite and martensite. *Trans. AIME* **197,** 203 (1953).

35. M. Ron: *Applications of Mössbauer Spectroscopy*, Vol. II (Academic Press, New York, 1980), pp. 335-340.

36. S. Kachi, Y. Bando, and S. Higuchi: The phase transformation of iron rich iron-nickel alloy in fine particles. *Jpn. J. Appl. Phys.* **1,** 307 (1962).

37. A. Jorio, M.A. Pimenta, A.G. Souza Filho, R. Saito, G. Dresselhaus, and M.S. Dresselhaus: Characterizing carbon nanotube samples with resonance Raman scattering. *New J. Phys.* **5,** 1391 (2003).

38. N.M. Rodriguez: A review of catalytically grown carbon nanofibers. *J. Mater. Res.* **8,** 3233 (1993).

39. Ch. Laurent, E. Flahaut, A. Peigney, and A. Rousset: Metal nanoparticles for the catalytic synthesis of carbon nanotubes. *New J. Chem.* **22,** 1229 (1998).

40. J.H. Hafner, M.J. Bronikowski, B.K. Azamian, P. Nikolaev, A.G. Rinzler, D.T. Colbert, K.A. Smith, and R.E. Smalley: Catalytic growth of single-wall carbon nanotubes from metal particles. *Chem. Phys. Lett.* **296,** 195 (1998).

41. E. Flahaut, A. Peigney, Ch. Laurent, and A. Rousset: Synthesis of single-walled carbon nanotube-Co-MgO composite powders and extraction of the nanotubes. *J. Mater. Chem.* **10,** 249 (2000).

42. R.R. Bacsa, Ch. Laurent, A. Peigney, W.S. Bacsa, Th. Vaugien, and A. Rousset: High specific surface area carbon nanotubes from catalytic chemical vapor deposition process. *Chem. Phys. Lett.* **323,** 566 (2000).

43. K. Hernadi, A. Fonseca, J.B. Nagy, A. Siska, and I. Kiricsi: Production of nanotubes by the catalytic decomposition of different carbon-containing compounds. *Appl. Catal. Gen.* **199,** 245 (2000).

44. F.L. Garcia, A. Peigney, and Ch. Laurent: Tetragonal-(Zr,Co)O_2 solid solution: Combustion synthesis, thermal stability in air and reduction in H_2, H_2-CH_4 and H_2-C_2H_4 atmospheres. *Mater. Res. Bull.* **43,** 3088 (2008).

45. G. Luo, Z. Li, F. Wei, L. Xiang, X. Deng, and Y. Jin: Catalysts effect on morphology of carbon nanotubes prepared by catalytic chemical vapor deposition in a nano-agglomerate bed. *Physica B (Amsterdam)* **323,** 314 (2002).

46. W. Qian, T. Liu, Z. Wang, H. Yu, Z. Li, F. Wei, and G. Luo: Effect of adding nickel to iron-alumina on the morphology of as-grown carbon nanotubes. *Carbon* **41,** 2487 (2003).

47. M. Yamada, M. Kawana, and M. Miyake: Synthesis and diameter control of multi-walled carbon nanotubes over gold nanoparticle catalysts. *Appl. Catal. Gen.* **302,** 201 (2006).

48. K.Y. Tran, B. Heinrichs, J-F. Colomer, J-P. Pirard, and S. Lambert: Carbon nanotubes synthesis by the ethylene chemical catalytic vapour deposition (CCVD) process on Fe, Co, and Fe-Co/Al_2O_3 sol-gel catalysts. *Appl. Catal. Gen.* **318,** 63 (2007).

49. W. Qian, T. Liu, F. Wei, Z. Wang, G. Luo, H. Yu, and Z. Li: The evaluation of the gross defects of carbon nanotubes in a continuous CVD process. *Carbon* **41,** 2613 (2003).

50. S. McCaldin, M. Bououdina, D.M. Grant, and G.S. Walker: The effect of processing conditions on carbon nanostructures formed on an iron-based catalysts. *Carbon* **44,** 2273 (2006).